THE HIRENASD PROJECT:

HIGH REYNOLDS NUMBER AEROSTRUCTURAL DYNAMICS EXPERIMENTS IN THE EUROPEAN TRANSONIC WINDTUNNEL (ETW)

J. Ballmann, A. Dafnis, C. Braun, H. Korsch, H.-G. Reimerdes, H. Olivier
RWTH Aachen University
Templergraben 55, D - 52062 Aachen, Germany

Keywords: *Transonic Flow, High Reynolds Numbers, Experimental/Computational Aeroelasticity*

Abstract

The paper gives an overview of an experimental high Reynolds number aerostructural dynamics project with forthcoming experiments in the European Transonic Windtunnel. Starting with the general approach during the wing model design, an overview of the measuring equipment, the dynamical qualifying of the windtunnel model, and numerical predictions by computational aeroelasticity are presented for the prepared windtunnel experiments.

1. Introduction

Transonic aeroelastic windtunnel testing with scaled wing models uses to be conducted hitherto in windtunnels at Reynolds numbers which are about one order of magnitude less than in real cruise flight of large passenger aircrafts. Only very few aeroelastic windtunnel experiments with oscillating elastic wings have been performed, so far, in the transonic flow regime at flight Reynolds numbers of large transport aircrafts [1], even though the transonic regime is characterised by strong nonlinearities with shocks and phenomena which strongly depend on the Reynolds number. Besides the necessity for a thorough understanding of aeroelastic phenomena, windtunnel experiments with elastic wings are necessary to validate methods for computational aeroelastic simulation (CAS) of elastic airplane flight and multidisciplinary airplane design, but normally those data is declared confidential and not open to university research.

The objectives of the High Reynolds Number Aerostructural Dynamics project (HIRENASD) are to improve the aero-structural dynamics understanding and knowledge in the transonic regime at Reynolds numbers of real transport aircrafts and to gather experimental data in a wide range of Reynolds numbers and aerodynamic loads for current and future aeroelastic research. Under cryogenic conditions, it is possible in the European Transonic Windtunnel (ETW) to achieve Reynolds numbers of up to 80 millions at transonic Mach numbers, similar to the conditions mentioned above, see Fig. 1. A further advantage of ETW is that the parameters Mach number, Reynolds number, and dynamic pressure (or even more adequate the ratio of pressure to Youngs modulus of the model material), which are influencing the aeroelastic behavior of the wing, can be varied independently.

In the experiments, now scheduled for August/September 2006, emphasis is put on transonic flow about aeroelastic equilibrium configurations of an elastic supercritical wing model, aero-structural dynamic processes during vibration excitation, aerodynamic damping mechanisms, unsteady shock/boundary-layer interaction and unsteady flow separation up to buffeting onset. One of the test envelopes chosen for the forthcoming tests is presented in Fig. 2.

The chosen profile of the swept elastic windtunnel model corresponds to the BAC 3-11/RES/30/21 cruise flight profile which is supercritical and has 11 % thickness [2], [3]. The planform of the first design of the model corresponded to the SFB 401 clean wing reference configuration [3] which is shown in Fig. 3. In the first wing section from the root the profile thickness was modified such that it varies linearly from 15 % at the root to 11 % at the transition to the second section. That increment of the profile thickness is completely restricted to the first section and placed on the pressure side of the wing. Only there the profile deviates from the BAC 3-11 airfoil, see bottom of Fig. 3.

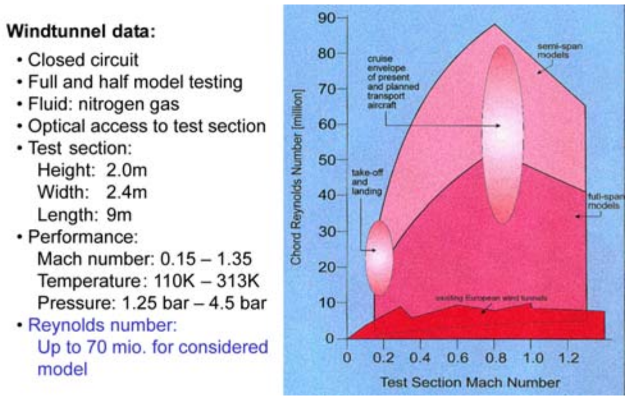

Windtunnel data:

- Closed circuit
- Full and half model testing
- Fluid: nitrogen gas
- Optical access to test section
- Test section:
  Height: 2.0m
  Width: 2.4m
  Length: 9m
- Performance:
  Mach number: 0.15 – 1.35
  Temperature: 110K – 313K
  Pressure: 1.25 bar – 4.5 bar
- Reynolds number:
  Up to 70 mio. for considered model

Fig. 1: Envelope of the experimental conditions in the European Transonic Windtunnel (ETW) compared with common windtunnels

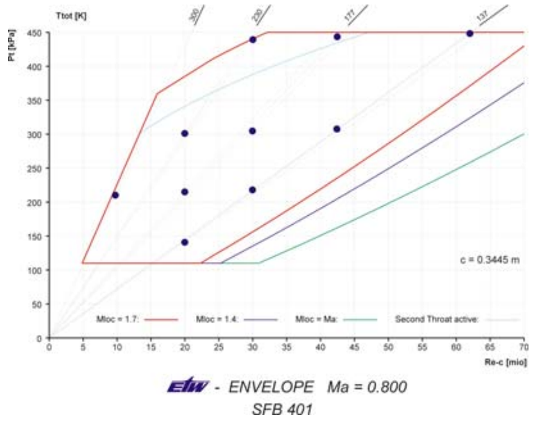

Fig. 2: One of three HIRENASD test envelopes, windtunnel conditions are marked with circles

Contributions to the design of the elastic wind tunnel model have been made by different sub-projects of SFB 401 to meet required aeroelastic properties in consideration of the multidisciplinary aspects. Computer aided geometrical design (CAGD) tools [4] have been used for the design of the outer surface of the model and converted to CAD data applying the CATIA software. The dynamic dimensioning was mainly focused on clearly separated eigenmodes and frequencies. In each design step the structural properties of the wing model were computed using Computational Structural Dynamics (CSD) methods, while a Navier-Stokes solver delivered the aerodynamic loads. The fully coupled fluid-structure interaction method SOFIA [5], [6], [7], [8], which is still being further developed in SFB 401, has been extensively applied to predict the steady and unsteady aeroelastic behavior of the model under windtunnel conditions.

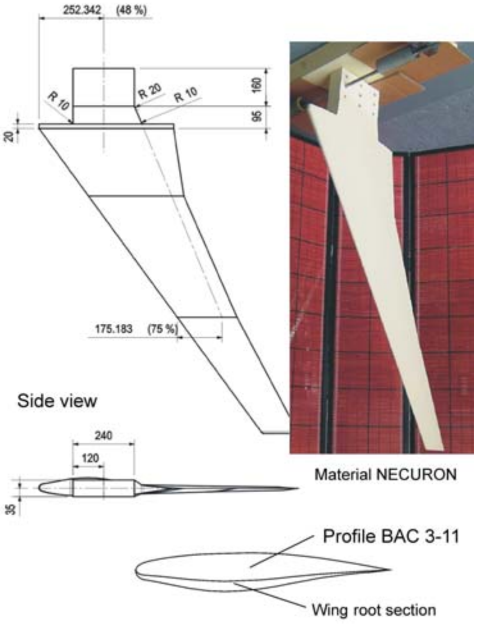

Fig. 3: Wing model geometry 1^{st} design and CNC 1:1 milling from a view model material (top right)

2. Windtunnel Model Assembly

2.1. Wing Model Geometry and Material

The planform of the manufactured elastic wing model has the typical characteristics of a wing for a large passenger aircraft. The leading edge sweep angle is 34°, the span of the model is 1285.71 mm, and the chord decreases from its root value over three sections piecewise linearly to the tip value. Fig. 4 contains the chord length values at the three wing-section transitions which vary from 549.31 mm at the wing root to 149.29 mm at the wing tip. The aerodynamic mean chord and planview wing area are C_{ref} = 0.3445 m and A_{ref} = 0.39255 m². The profile thickness distribution of the first design was kept as explained in the introduction.

In order to realise the highest Reynolds numbers, the flow medium nitrogen has to be cooled down to about 120 K, and the windtunnel total pressure has to be rised to about 400 kPa, see Fig. 2. These conditions result in a dynamic pressure of up to 130 kPa at transonic Mach numbers. Therefore a highly tenacious material is needed for the elastic model which endures dynamic loading over the full range of dynamic pressure and temperature according to the envelopes of the experiments. The material of choice was a C200 Maraging steel (G90c) with 18° Nickel [9].

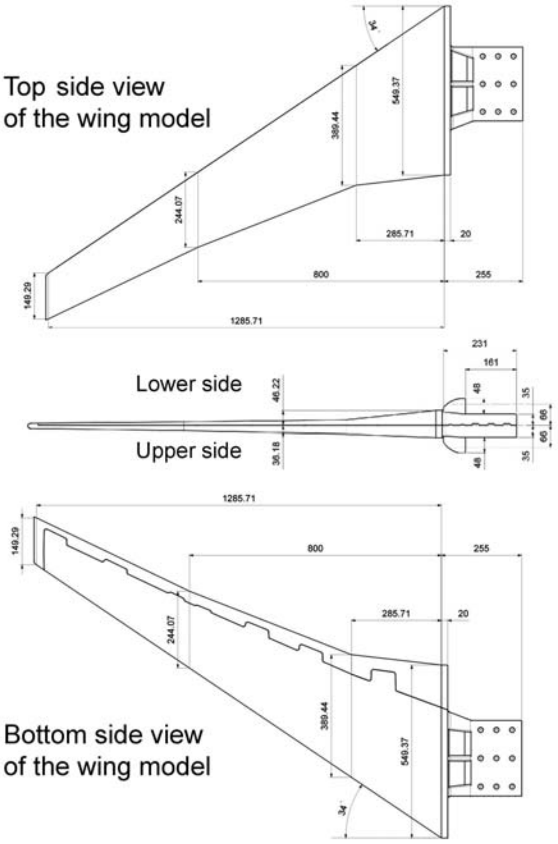

Fig. 4: Geometry of the final design of the SFB 401 windtunnel model for experiments in ETW, aerodynamic mean chord amc=0.3445 m

The model consists of two pieces, the upper and the lower part which have a jointing surface with straight separation line along the leading ledge and a meandering separation line on the bottom surface of the model, as can be seen on the bottom side view of the wing model in Fig. 4. To impede relative motion of the model parts, a growed and tongued joint concept has been applied in span- and cross-direction along the jointing surface. This can be seen in Fig. 5, which shows the interior of the top and bottom parts of the wing model, where one can recognise seven ribs for implementation of pressure sensors and three stringers in longitudinal direction, of which the central ends at about 60 % span.

To test the chosen contact surface concept with notches and teeth, a smaller two-piece pre-model had been prepared and tested with respect to high cycle fatigue, fracture toughness of the mounting bolts and influence of dry friction contact phenomena, like e.g. stick slip motion. There was no negative effect observed, the pre-model behaved much like a one-piece model.

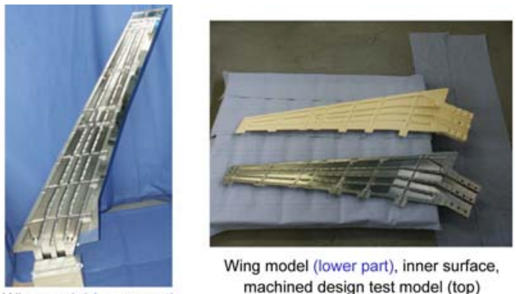

Wing model (upper part), inner surface

Wing model (lower part), inner surface, machined design test model (top) and windtunnel model (bottom)

Fig. 5: Interior of the windtunnel model before measuring installation

2.2. Fuselage Substitute

In order to alleviate the influence of the ceiling boundary layer of the windtunnel, where the model will be mounted on a plate at the turntable for half-model testing, a fuselage substitute is provided around the wing. It will have no mechanical contact with the elastic wing model (see Fig. 6 and Fig. 7). A round arch labyrinth sealing is implemented on the fuselage substitute side which surrounds the wing root. Thus the complete wetted surface in the windtunnel looks much like a wing body half-configuration.

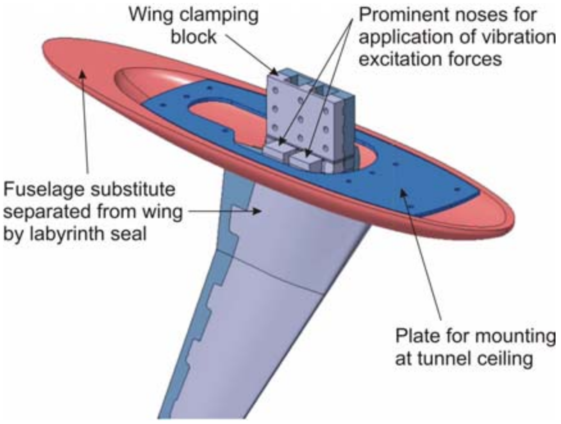

Fig. 6: Wing assembly inside the windtunnel

Fig. 7: Fuselage substitute, flow side, labyrinth seal provided around the opening for the wing

Flow computation has been first performed for the jig shape, i.e. ignoring the wing deformation. Fig. 8 and Fig. 9 show the surface grid and the pressure distribution on the wetted surface together with some streamlines for one windtunnel condition of the forthcoming experiments. The labyrinth gap was ignored in the flow simulation. Aeroelastic simulations for this configuration are presently in progress, using the SOFIA code. The fuselage substitute is assumed undeformable.

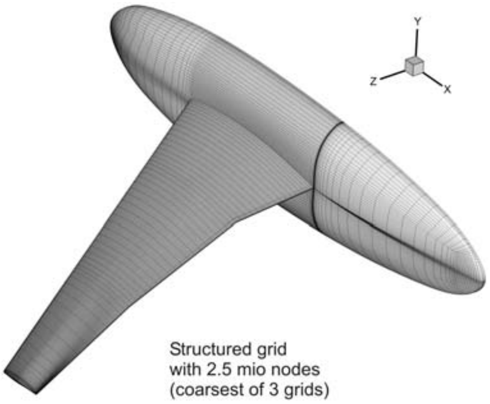

Fig. 8: Surface grid for the wing fuselage-substitute assembly, every second grid line omitted.

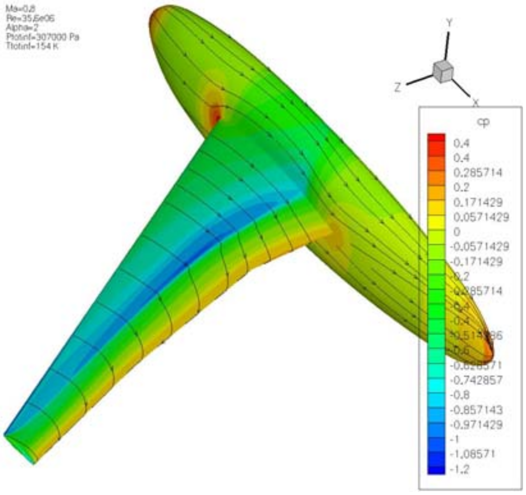

Fig. 9: Pressure distribution and streamlines for Ma_∞=0.8. angle of attack α=2°, Re=$35.6\cdot10^6$, computation on grid with 3.5 mio nodes, wing deformation ignored.

2.3. Vibration Excitation Mechnism

Vibration excitation will be performed near resonance for the two lowest bending modes which represent predominantly flap bending and the first torsion-dominated mode. The mode shapes and frequencies have been computated using two different finite element codes with volume discretisation and one based on the multiaxial Timoshenko beam model, using the appropriate finite element discretisation implemented in the SOFIA code. Results were very much the same and are presented in Fig. 10 for one of the computations. But it must be mentioned that modelling of the elastic wing did presently not care about the jointing of the two parts, and no friction in the jointing surface of the wing model nor any dynamical influence of the measurement implementation including the signal cables were taken into account. For this reason the presently calculated frequencies are higher than in the free vibration tests without wind.

Forced vibration of the windtunnel model is realised by dynamic force couples made up by four spanwise directed forces which are applied at respective prominent noses at the wing root, which are indicated in Fig. 6 and can also be seen in Fig. 11 and Fig. 12. The forces are produced by four pre-stressed piezo-stacks, mounted in a containment which is very stiff and forms one piece with the wing clamping. Therefore these forces are interior forces, acting within the assembly, which is composed of the wing and the vibration excitation mechanism. The excitation forces are transmitted by stacks, which, for thermal extension reasons, are made from the same material as the wing model, as well as the excitation mechanism containment.

Fig. 10: Two first bending and first torsion mode shapes and eigenfrequencies

Fig. 11: Wing model assembly during mounting for dynamic qualification in the laboratory; in the foreground one of the four excitation piezo stacks

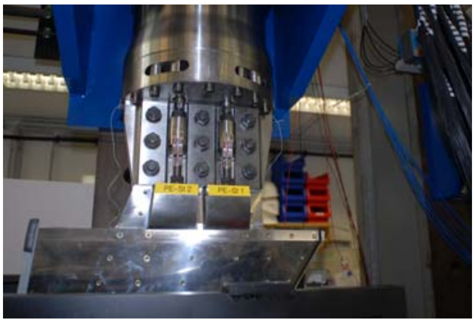

Fig. 12: Wing model with excitation mechanism in the dynamics laboratory

3. Measuring Equipment

3.1. Force Measurement

Within the HIRENASD project, a new windtunnel balance (see Fig. 13) had to be made for measuring during the dynamical aeroelastic experiments, because the present windtunnel balance in ETW has been designed for stationary testing and is by far not stiff enough for dynamic measurements. The lowest eigenmodes of the new balance are in the range of 1000 Hz.

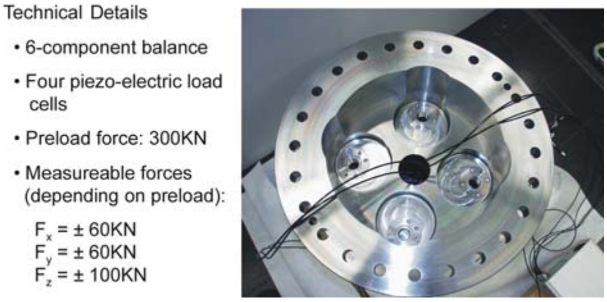

Technical Details

- 6-component balance
- Four piezo-electric load cells
- Preload force: 300KN
- Measureable forces (depending on preload):

$F_x = \pm 60KN$
$F_y = \pm 60KN$
$F_z = \pm 100KN$

Fig. 13: Inside view of the piezo-6 components windtunnel balance

3.2. Pressure Sensors

For testing the selected cryogenic miniature/ultraminiature pressure sensors (Kulites) under cryogenic conditions, an airfoil with the reference profile BAC 3-11 was manufactured from the cryogenic material chosen for the ETW wing model and examined in the windtunnel KRG of DLR Göttingen. The airfoil chord length was 150 mm and its span 400 mm. It was instrumented with 41 Kulite pressure sensors along the middle cross-section. Fig. 14 shows some time histories of signals of pressure sensors during an experiment and, in the middle, the arrangement of the sensors and pressure holes along the cross-section. The middle part with mean-pressure plateau corresponds to the measuring time.

In the two experiments referred to in Fig. 15, buffet has been observed. The flow conditions are in both cases the same for Mach number Ma=0.75 and angle of attack α=4°, but with different Reynolds numbers, namely Re=4.85 millions (stagnation temperature 262.5 K) for experiment No. 60 and Re=16.18 millions (stagnation temperature 148.5 K) for experiment No.

179. Like in the series of experiments reported in [10], experiment No. 179 was performed under cryogenic conditions. The buffet frequencies observed were 128 Hz in the lower and 88 Hz in the higher Reynolds number case. Fig. 15 shows for both experiments the upper most and the down most positions of the shock during buffet.

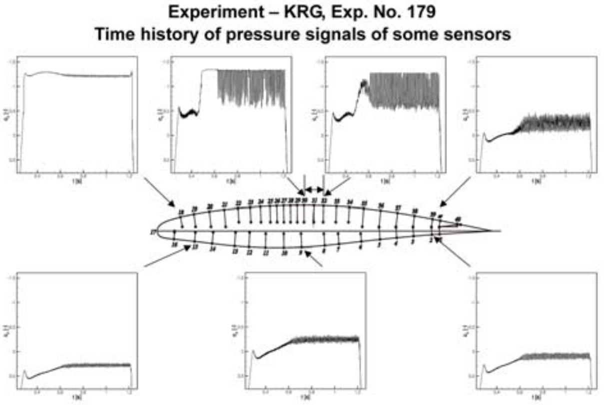

Fig. 14: Time history of pressure for a buffet case under cryogenic conditions, Ma_∞=0.75, α=4°, Re=18,16·10^6.

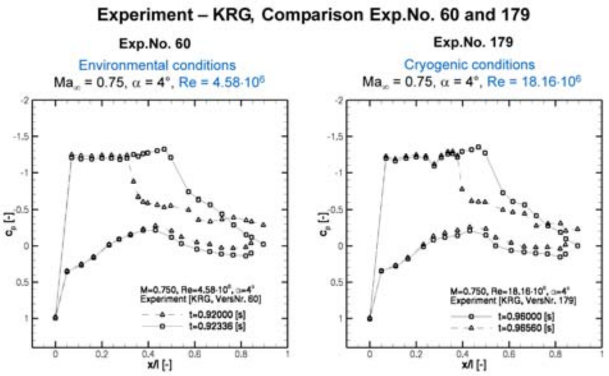

Fig. 15: Two instantaneous pressure distributions in buffet cases at different Reynolds numbers.

The HIRENASD wing model has been equipped with 259 cryogenic miniature/ultraminiature pressure sensors (Kulites) which are implemented in 7 spanwise cross-sections. The relative span positions η of these 7 cross-sections and the respective numbers of sensors are (see also Fig. 16) as follows:

section	1	2	3	4	5	6	7
η	0.14	0.32	0.46	0.59	0.66	0.80	0.95
number	43	41	40	38	35	31	31

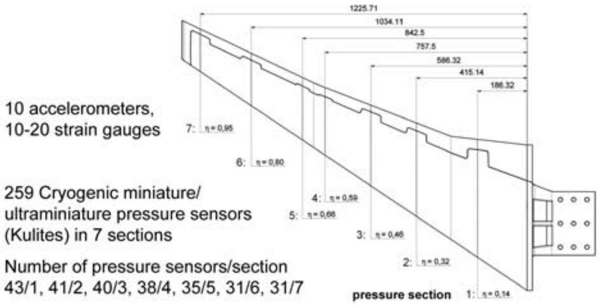

Fig. 16: Pressure sensor equipment

Because of place requirements for the sensors in the interior of the wing, the sensors and pressure holes on the bottom side of the wing model are about 2 mm shifted towards the tip, relative to the pressure holes on the model top side. The photograph in Fig. 17 shows the complete sensor equipment after implementation.

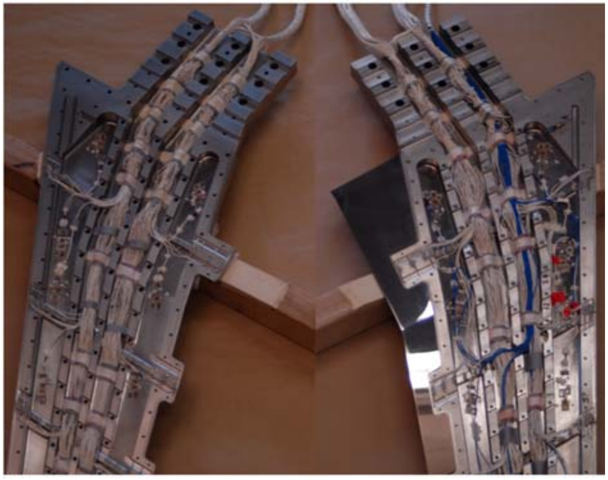

Fig. 17: Sensor installation inside the suction and pressure side parts of the model. Wiring colors: thick white belong to pressure sensors, thin white to strain gauges, blue to accelerometers.

3.3. Strain Measurements

The windtunnel model assembly will be equipped with 28 strain gauges, of which 22 are distributed in the wing model (see Fig. 18) and the rest in the excitation mechanism. Fig. 20 gives a close view of one strain gauge implementation, together with two accelerometers.

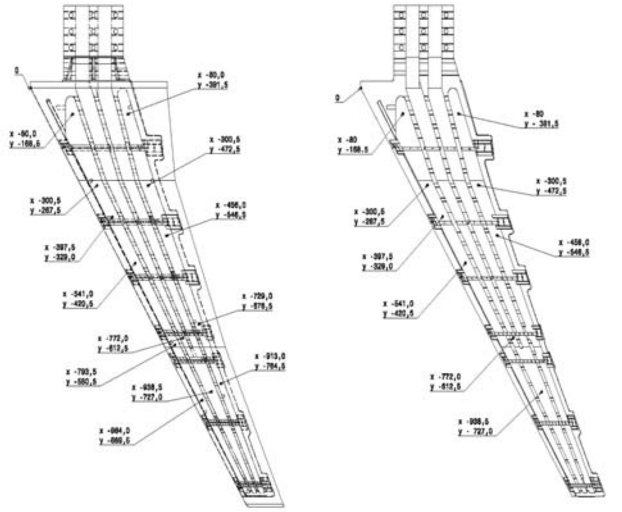

Fig. 18: Positions of 22 strain gauges in the interior of the wing model; Cartesian coordinates in mm, origin: point 0 at wing root

3.4. Acceleration Measurements

For monitoring acceleration during the vibration tests 11 accelerometers have been implemented, all in the upper part of the wing model (suction side). Fig. 19 indicates the positions of these sensors.

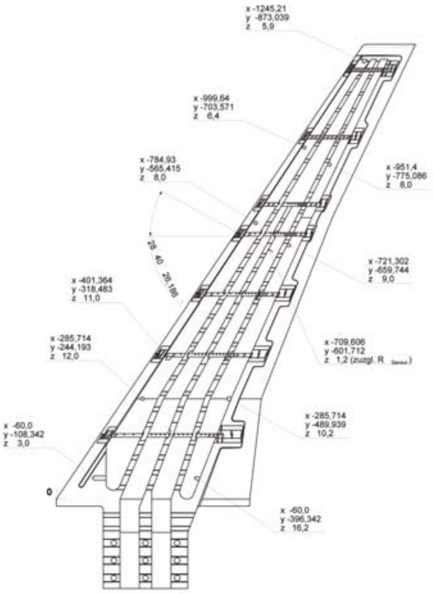

Fig. 19: Positions of accelerometers; Cartesian coordinates in mm, origin: point 0 at wing root

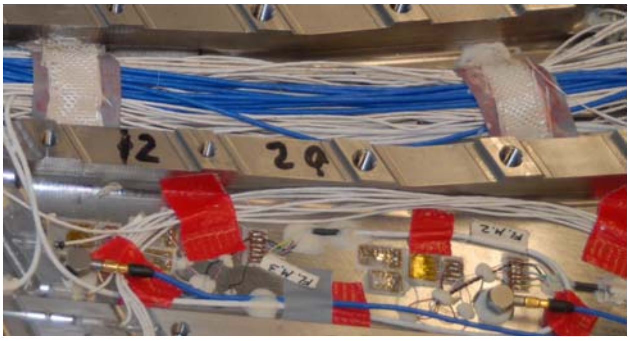

Fig. 20: Close view of sensor application in the suction side part, showing accelerometer and strain gauge applications

3.5. Measurement of Surface Movement

High speed video imaging will be employed for 3D-stereo tracking of an arrangement of markers (see Fig. 21), which are implemented on the bottom surface of the wing model. For this the position of the undeformed wing is defined first in a virtual coordinate frame, using a cuboidal frame with light points. (see Fig. 22). Ultra-high speed frame grabbing allows recording of the deformation history of the wing during vibration.

Fig. 21: Complete windtunnel assembly from balance (top) to clamping and wing model equipped with markers for dynamical pre-tests.

Fig. 22: Cuboidal frame for defining the virtual position reference system

4. Dynamical Qualifying of the Model

Presently, the dynamical qualification is performed in the laboratory, without wind. It includes measuring of mode frequencies, damping characteristics and mode shapes as well as excited vibration tests. At the same time the complete measuring installation is checked for correct functioning. The measured mode frequencies arrived a little lower than in the computations within which material damping and contact mechanics in the jointing surface were ignored.

5. Preliminary Aeroelastic Predictions of Experimental Results

Before the windtunnel experiments, for a part of the test conditions in ETW, numerical simulations have been performed in advance using the SOFIA code. Some of these blind test predictions are presented in this section. In the computations the fuselage substitute was still excluded. Also wall boundary conditions did not jet correspond correctly to the windtunnel situation, because the root cross-section plane is supposed to be a symmetry plane without viscosity.

5.1. Prediction of Aeroelastic Equilibrium Configurations

Results of a static aeroelastic simulation with angle of attack α=2° are presented in Fig. 23 and Fig. 24 for Mach number Ma=0.8 and Reynolds number $Re=35\cdot10^6$. The simulation runs completely in the fluid-structure coupled fashion and needed about 3 % more computer time than for the pure aerodynamic part when deformation is ignored. Fig. 23 shows the pressure distribution on the deformed wing in its aeroelastostatic equilibrium configuration.

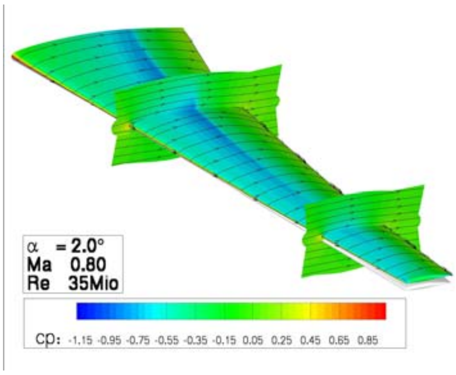

Fig. 23: Pressure distribution and streamlines, computation on grid with 1.2 mio nodes; deformed wing in aeroelastic equilibrium configuration

Fig. 24 presents c_p distributions in different wing sections when deformation is ignored and when it is taken into account. The graphs indicate the differences increasing with span. Accordingly the lift of the deformed wing comes out lower than the lift of the undeformed wing.

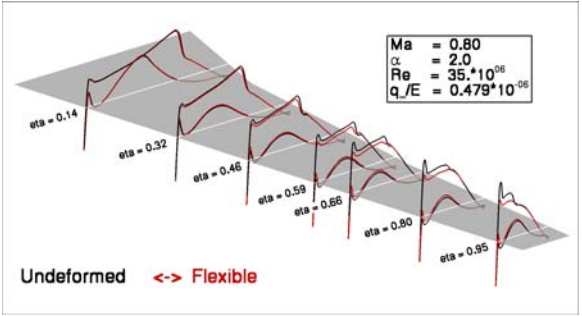

Fig. 24: Comparison of pressure coefficient in spanwise sections without and with deformation

Fig. 25 shows the change of lift over angle of attack for the elastic wing in the steady flow case for different values of dynamic pressure q and consequently q/E, where E is the elastic modulus, which weakly depends on temperature. The diagram shows that the lift of the deformed wing in its aeroelastic equilibrium configuration has lower values than the lift of the wing in its undeformed (jig) shape and decreases with increasing q/E. It should be remarked here that for angles of attack greater than +4° flow separation occurs which is not well predicted by the used Reynolds averadged Navier-Stokes code.

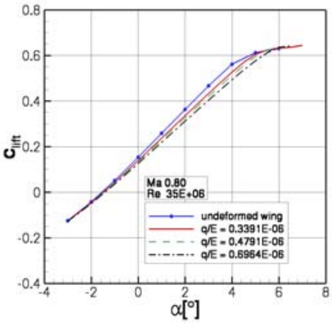

Fig. 25: Influence of q/E on lift over angle of attack; deformed wing model in aeroelastic equilibrium configuration

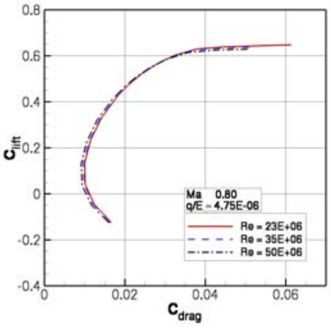

Fig. 26: Reynolds number influence on lift over drag polar; deformed wing model in aeroelastic equilibrium configuration

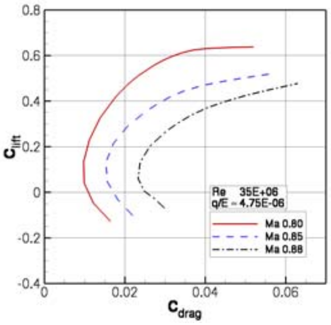

Fig. 27: Mach number influence on lift over drag polar; deformed wing model in aeroelastic equilibrium configuration

Fig. 26 presents aeroelastic equilibrium results of lift over drag polars at fixed values of Mach number and q/E for three different Reynolds numbers. For the higher Reynolds numbers $35 \cdot 10^6$ and $50 \cdot 10^6$, the changes of the polars with Reynolds number came out relatively small over the full simulated angle of attack range from –3° to +6°.

The influence of Mach number on the lift over drag polar at fixed Reynolds number and q/E is relatively strong, as expected, and can be seen in Fig. 27.

5.2. Prediction of Free Vibration Test

The diagram of Fig. 28 exhibits the deformation motion of the wing, represented by tip displacement and torsion angle at tip. The computation starts from the equilibrium configuration of the elastic wing, which results from aerodynamics and an additional loading at the tip of the wing, after removing the additional loading. The chosen stationary flow conditions were Ma=0.8, α=0°, $Re=35 \cdot 10^6$ and $q/E=0.479 \cdot 10^{-6}$. The additional external loading was formed by a tip up load of +1200 N applied on the elastic axis and a nose down torque of 50 Nm.

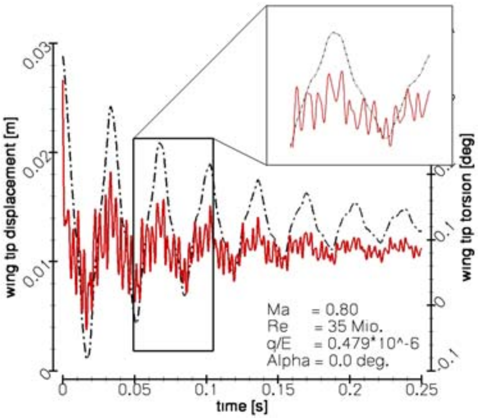

Fig. 28: Blind numerical prediction of a free vibration test under wind represented by tip vertical and torsional oscillation history.

The obviously strong decrease of the vibration amplitudes with time is caused by viscosity and energy radiation into the fluid. The vibration frequency is shifted due to wind about + 2 to 3 Hz for the two first bending and about – 0.2 Hz for the first torsion mode.

5.3. Prediction of a Dynamic Excitation Test

A time-dependent in plane force couple formed by the piezo-stacks in the excitation mechanism, with absolute value 10 kN in each stack, has been applied with the torsion-dominated resonance frequency 272.4 Hz of the Timoshenko beam model. This mode is excited almost linearly first, and after the time of 0.08 s the simulation exhibits a decreasing rate of rise of the amplitude, which is due to the fluid structure interaction, see Fig. 29.

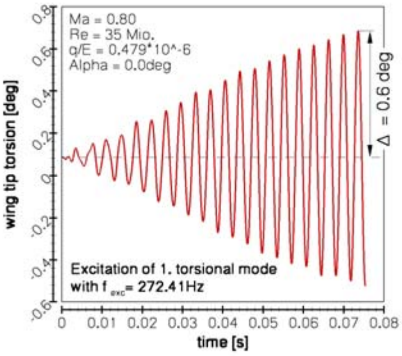

Fig. 29: Blind numerical prediction of an excited vibration test under wind.

6. Acknowledgement and Invitation

The funding by the German Research Foundation (DFG) of the project within the frame of the collaborative research center and SFB 401 “Flow Modulation and Fluid-Structure Interaction at Airplane Wings” is gratefully acknowledged. The authors thank Airbus Industry for supporting the development of the new balance, the German Aerospace Center (DLR) and ETW for continuous advice. The aeroelastic community is invited to visit the homepage http:// www.lufmech.rwth-aachen.de/HIRENASD/ to get detailed information about the geometry and data of the windtunnel assembly as well as planned windtunnel conditions and to produce blind test predictions. We would like to include these in our data base, which, with respect to the experimental data, will successively be opened to the community.

7. Literature

[1] Cole, S.R., Noll, T.E., Perry, B. III: Transonic Dynamics Tunnel Aeroelastic Testing in Support of Aircraft Development. Journal of Aircraft, Vol. 40, No. 5, 2003

[2] Özger, E., Schell, I., Jacob, D.: On the Structure and Attenuation of an Aircraft Wake. AIAA Journal of Aircraft, Vol. 38, No. 5, pp. 878-887, 2001

[3] Moir, I.-R.M. Measurements on a two-dimensional aerofoil with high-lift devices. AGARD-AR-303, Vol. II, 58-59, 1994

[4] Brakhage, K.-H., Lamby, Ph.: CAGD Tools for High Quality Grid Generation and Sparse Representation. Proceedings of the 8th International Conference on Numerical Grid Generation in Computational Field Simulations, Waikiki Beach, Hawaii. Ed.: B.K. Soni, J.F. Thompson, J. Häuser, P. Eiseman, pp 599-608, 2002

[5] Ballmann J. (Ed.): Flow Modulation and Fluid-Structure-Interaction at Airplane wings. Notes On Numerical Fluid Mechanics And Multidisciplinary Design, Vol. 84, pp. 105-122, 2003

[6] Kämpchen, M., Dafnis, A., Reimerdes, H.-G., Britten, G., Ballmann, J.: Dynamic Aero-Structural Response of an Elastic Wing Model. Journal of Fluids and Structures, Vol. 18, pp. 63-77, 2003

[7] Braun, C., Boucke, A., Ballmann, J.: Numerical Prediction of Wing Deformation of a High Speed Transport Aircraft Type Wind Tunnel Model by Direct Aeroelastic Simulation. IFASD 2005, Munich, Germany, paper IF 147

[8] Reimer, L.: Analysis of the Static and Dynamic Aero-Structural Response of an Elastic Swept Wing Model by Direct Aeroelastic Simulation, ICAS 2006, Paper 10.3.3

[9] Wigley, D. A. (prep.): ETW Materials Guide Document ETW/D/95005, Köln 1996

[10] Bartels, R.E., Edwards, J.W.: Cryogenic Tunnel Pressure Measurements on a Supercritical Airfoil for Several Shock Buffet Conditions. NASA TM-110272, 1997